Correlating structure and orbital occupation with the stability and mechanical properties of 3d transition metal carbides

I. Khatri [a], N.J. Szymanski [a,b], B.B. Dumre [a], J.G. Amar [a], D. Gall [c], S.V. Khare [a,*]

[a] *Department of Physics and Astronomy, University of Toledo, Toledo, OH 43606, USA*
[b] *Department of Materials Science and Engineering, University of California, Berkeley, Berkeley, CA 94720, USA*
[c] *Department of Materials Science and Engineering, Rensselaer Polytechnic Institute, Troy, NY 12180, USA*

ARTICLE INFO

ABSTRACT

The development of novel transition metal carbides for improved hard coating technologies requires a detailed understanding of the factors influencing their stability and mechanical performance. To this end, we carried out first principles calculations based on density functional theory to tabulate the electronic structures, formation energies, and phonon dispersion curves of 3d transition metal carbides adopting zincblende, rocksalt, and cesium chloride structures. By analyzing the corresponding results, we outline a theoretical framework that describes how valence electron concentration and bonding configuration control the stability of these compounds. Many early transition metal carbides are predicted to be stable in the rocksalt and zincblende structures, enabled by filled bonding states, whereas the cesium chloride structure shows persistent instability. For compounds that are predicted to be stable, mechanical properties were investigated through calculation of elastic tensors, from which observable properties including Vicker's hardness and ductility were derived. A robust mechanical performance is shown to be correlated with complete filling of bonding orbitals as illustrated for rocksalt TiC and VC, which have calculated hardnesses of 25.66 and 22.63 GPa respectively. However, enhanced ductility and toughness can be achieved by allowing partial occupation of the antibonding states as in CrC, which has a relatively low Pugh's ratio of 0.51.

© 2021 Elsevier B.V. All rights reserved.

1. Introduction

Many transition metal carbides (TMCs), nitrides, and carbonitrides are known to display a wide range of remarkable physical and chemical properties [1–15]. These include but are not limited to exceptional hardness and wear resistance, robust stability at high operating temperatures, and high thermal conductivity [4]. Moreover, TMCs have been the subject of intense research interest in the fields of catalysis and surface science [16]. Detailed reviews of previous work on well-studied TMCs and their alloys can be found in Refs. [4–23]. Owing to their versatile properties, several TMCs have been considered for industrial applications involving hard coatings [24,25], refractory materials, conducting barriers, energy storage devices [26,27], catalytic agents [28], and potentially even high-temperature superconductors [29]. Depending on the application in focus, many previous studies have aimed to study the electronic structure and its influence on the bonding characteristics of the

TMCs [9,19,30]. Because the underlying electronic structure may be tuned using both structure and composition, it is possible to fine-tune the materials by design. However, this requires a detailed understanding of the correlation between atomic-level electronic interactions and macroscopic properties. We therefore aim to build upon previous work [31,32] to illustrate a clear framework describing the factors influencing the stability and mechanical performance of TMCs.

Numerous studies have been conducted on TMCs using both experimental [33–36] and theoretical techniques, primarily focusing on the rocksalt structure which is most commonly adopted by these compounds [37–54]. With respect to their mechanical properties, Balasubramanian et al. [31] identified the valence electron concentration as a dominant factor controlling hardness and ductility across many rocksalt TMCs based on orbital filling. Using similar arguments, Häglund et al. [11] found that the cohesive energy in 3d TMCs is correlated with the filling of bonding and antibonding orbitals, with TiC showing the most exothermic cohesive energy of all compounds considered. Moving toward TMCs with higher group numbers, Singh et al. [42] reported that instability arises as metal-carbon bonds become weakened upon the increased filling of the

antibonding orbitals, e.g., in CrC. This effect becomes more pronounced when dealing with the intermediate and late TMCs (FeC, CoC, and NiC), where previously reported mechanical properties imply relatively weak bonding [45].

While there has been extensive work done involving TMCs, a detailed and systematic investigation of 3d TMCs has not yet been reported across three unique cubic structures: rocksalt (RS), zinc-blende (ZB), and cesium chloride (CsCl). Here, we address this shortcoming by presenting the results of first principles calculations based on density functional theory. We specifically choose to focus on the electronic structures, formation energies, and phonon dispersion curves calculated for all ten 3d TMCs. We restrict our main analysis to cubic structures as those are suspected to balance good hardness and ductility, whereas materials with a hexagonal (wurtzite) structure tend to be brittle owing to a lack of slip planes [55,56]. Our calculated results comprise a theoretical guide that may be used to understand how valence electron concentration and bonding configuration each play a role in the stability of these compounds. In addition, we have also studied the mechanical properties of compounds that are predicted to be stable using calculated elastic tensors. Derived properties are then considered to reveal insight into the performance of the TMCs for hard coating applications.

In summary, we present results that imply the stability of seven TMCs in the ZB structure and five in the RS structure, whereas a persistent instability is observed in the CsCl configuration owing to its dense eight-fold coordination. As for the instabilities that arise through intermediate TMCs in the RS structure, metallic dimers are predicted to form as a direct result of strong d-d orbital overlap. This occurs due to an increased valence electron concentration, as well as a decrease in the metal−carbon bond strengths. In contrast, instabilities in the ZB structure are attributed to Jahn-Teller distortions [57–59] mediated by degenerate d orbital configurations in the tetrahedral ligand field. For the stable compounds, an increasing valence electron concentration leads to higher values of C_{11} and C_{12}, which in turn raises the bulk moduli across intermediate TMCs. In comparing RS versus ZB structures, the former is found to lead to higher shear resistance (and therefore much higher hardness) given that its bonding configuration enforces strong d-p orbital hybridization. From these results, we conclude that early TMCs adopting the RS structure are preferred for hard coating applications, confirming previous findings and removing the need for further investigation regarding alternative structures and compositions for this purpose. Among these compounds, a tradeoff is illustrated between hardness and ductility, which are predicted to be optimal in TiC and CrC respectively.

2. Computational methods

All density functional theory (DFT) calculations were carried out using the Vienna Ab initio Simulation package (VASP) [60–63]. The projector augmented wave (PAW) [64] method was utilized with exchange-correlation interactions treated by the generalized gradient approximation (GGA) in the Perdew-Burke-Ernzerhof (PBE) formalism [65]. For the early 3d transition metals Sc, Ti, and V, semi-core s and p electrons were included as valence states, whereas only semi-core p electrons were included for Cr and Mn. Only outer-core electrons were explicitly considered in the late transition metals Fe, Co, Ni, Cu, and Zn. A plane-wave basis set was constructed using a kinetic energy cutoff of 520 eV. Γ-centered grids of 4000 k-points per reciprocal atom (KPPRA) were employed for all calculations in the Brillouin zone [66,67]. Electron minimizations, for which Gaussian smearing of width 0.05 eV was used, were performed with a convergence criterion of 10^{-6} eV/atom as in previous work [68–70]. Spin-polarization was taken into account for all compounds. Four possible magnetic configurations were tested with respect to the transition metal ions: (i) non-magnetic ordering with each moment

set to zero, (ii) ferromagnetic ordering with all moments aligned parallel, (iii) antiferromagnetic ordering with moments alternating along the [001] direction, and (iv) antiferromagnetic ordering with moments alternating along the [111] direction. For all compounds studied in this work, a non-magnetic or ferromagnetic configuration was identified to be the lowest-energy state – these ground states were used throughout the remainder of the calculations. Ionic relaxations were performed using a conjugate-gradient algorithm with a force constant criterion of 0.01 eV/Å as described in earlier works [71]. To precisely determine equilibrium lattice constants and bulk moduli, energies were computed for each compound at six volumes about the approximate energetic minima; these values were then fit to a Birch-Murnaghan equation of state [72,73].

To study the stability of each compound, we consider two key aspects: dynamics and energetics. Understanding the dynamical behavior of the structure is necessary to determine whether it is stable against perturbations; these include changes to the unit cell dimensions (strain), as well as collective atomic displacements (vibrational modes). To gain insight into the former, we calculated the independent elastic constants corresponding to the cubic crystal system (C_{11}, C_{12}, and C_{44}) by computing the energy of the unit cell under varied sets of strain and fitting the resulting values to a quadratic stress-strain relationship, as is described in detail throughout previous work [74–76]. From the elastic constants, stability against cell strain was determined using the Born criteria [77,78]:

$$C_{11} - C_{12} > 0, \ C_{11} + 2C_{12} > 0, \ \text{and} \ C_{44} > 0, \tag{1}$$

As for the effects of vibrational modes, we computed phonon dispersion curves along high-symmetry paths in the Brillouin zone. This was done by calculating the Hessian matrices for $5 \times 5 \times 5$ supercells using density functional perturbation theory (DFPT) [79] as implemented in VASP, with post-processing conducted via the PHONOPY [80] software. Compounds are deemed dynamically stable if all phonon frequencies are real, which implies that all atoms occupy positions corresponding to local energy minima. Should this condition hold, the next question is whether they are stable with respect to decomposition into competing phases, i.e., does the compound represent the energetic ground state. Here, we calculate the formation energy per atom of each binary carbide with respect to its constituent elemental ground states using the following equation:

$$\Delta E_F = \frac{E_{MC} - E_M - E_C}{2} \tag{2}$$

Accordingly, compounds with $\Delta E_F < 0$ are energetically preferable to the competing elemental phases, whereas compounds with $\Delta E_F > 0$ are energetically unstable. However, we note that such compounds may still be metastable assuming kinetic barriers are significant. The ground state structures of metal and carbon were used from Ref. [81].

To study the mechanical properties of the TMCs, we used the calculated elastic constants to obtain the bulk modulus (B), Cauchy pressure (P_c), shear modulus under the Voigt (G_V) and Reuss approximations (G_R) as well as Hill's arithmetic mean (G), Pugh's ratio (κ), Poisson's ratio (ν), and Young's modulus (Y) using the following equations:

$$B \ = \ (C_{11} + 2C_{12})/3 \tag{3}$$

$$P_c = C_{12} - C_{44} \tag{4}$$

$$G_V \ = \ [(C_{11} - C_{12}) + 3C_{44}]/5 \tag{5}$$

$$G_R = [5(C_{11} - C_{12})C_{44}]/(4C_{44} + 3C_{11} - 3C_{12}) \tag{6}$$

$$G \ = \ (G_V + G_R)/2 \tag{7}$$

$$\kappa = G/B \tag{8}$$

$$\nu = (3 - 2\kappa)/[2(3 + \kappa)] \tag{9}$$

$$Y = 9G/(3 + \kappa) \tag{10}$$

The Vickers hardness (H_V) was calculated using the following relation by Tian et al. [82]:

$$H_{\mathrm{V}} = 0.92\kappa^{1.137}G^{0.708} \tag{11}$$

The Debye temperature (θ_D) was also calculated via the following relations:

$$\theta_D = \frac{h}{k_B}\left[\frac{3n}{4\pi}\left(\frac{N_A}{M}\rho\right)\right]^{\frac{1}{3}}v_m \tag{12}$$

$$v_m = \left[\frac{2}{3}\left(\frac{2}{v_t^3} + \frac{1}{v_l^3}\right)\right]^{\frac{-1}{3}},$$

$$v_t = \left(\frac{G}{\rho}\right)^{\frac{1}{2}}, \quad v_l = \left(\frac{3B + 4G}{3\rho}\right)^{\frac{1}{2}} \tag{13}$$

where h is Planck's constant, k_B is Boltzmann's constant, N_A is Avogadro's number, ρ is the mass density, M is the molecular weight of the primitive cell, and n is the number of atoms in the cell for which M is calculated. v_t, v_l, and v_m are the transverse, longitudinal, and mean speeds of sound respectively.

To relate the macroscopic properties of TMCs to their underlying electronic structure, we calculated the density of states for each compound using the tetrahedron method with Blochl corrections [83]. Densities were further separated into elemental and orbital components to highlight the effects of the ligand field present in each structure. The ionic characters of individual bonds were revealed using metal-to-carbon charge transfer calculated within Bader's division scheme [84–86], which partitions real space to quantitatively attribute charge to each atom. On the other hand, covalent interactions were studied using Crystal Orbital Hamiltonian Populations (COHP) calculations performed with the LOBSTER package [87–91], which separates electronic occupancies into bonding and antibonding states.

3. Results and discussion

3.1. Structure and stability

The calculated volumes (per formula unit) of the 3d transitional metal carbides (TMCs) in the ZB, RS, and CsCl structures are listed in Table 1, showing excellent agreement with previously reported [92–94] data where available. Analyzing trends in volume with respect to structure, we observe an inverse correlation between the volume and the coordination number of the underlying atomic arrangement. Namely, $V_{ZB} > V_{RS} > V_{CsCl}$ owing to their respective coordination numbers of four, six, and eight. As for the effect of chemistry, there exists a nearly parabolic relationship between the volume and group number in all structures. This trend is directly related to the size of the metal element, which decreases from the early to intermediate TMs, then increases from intermediate to late TMs. As displayed in Fig. S1 of the Supplementary Material, subtle deviations from the parabolic relationship can be attributed to variations in the degree of bonding covalency versus ionicity [95]. Those elements with a large number of unpaired d electrons (e.g., Mn and Fe) tend to exhibit bond lengths representative of their covalent radii [95], whereas those with fewer unpaired electrons more clearly adopt highly ionic bonds.

Calculated lattice parameters and elastic constants are listed in Table S1 and S2 of the Supplemental Material respectively, and are in good agreement with available experimental [96–99] and calculated [100] values. The calculated elastic constants are used to determine whether each compound is mechanically stable, i.e., if they satisfy the Born criteria [77,78] and are therefore able to withstand strain without undergoing a phase transformation. We find twenty total compounds to be mechanically stable; these include eight ZB, ten RS, and two CsCl structures. Interestingly, there appears to be a clear difference in the origin of mechanical instability in the ZB and CsCl configurations – the former exhibits a lower value of C_{11} than C_{12}, whereas the latter exhibits a negative value of C_{44}. This suggests that the ZB structures are prone to instabilities arising from normal (uniaxial) strain, whereas CsCl structures are more likely to transform via shear strain. This agrees with expectations based on the connectivity of each structure - the ZB arrangement favors strong directional and shear-resistant bonding but is less robust against uniaxial compression owing to its low atomic density. In contrast, the CsCl structure is amenable to isotropic bonding, which is much more susceptible to shearing instabilities, while its high density is more resistant to normal strain. An intermediate situation is found in RS, which is commonly adopted by compounds formed via strong covalent (directional) and ionic (isotropic) bonding, including titanium carbides and nitrides which are known to be exceptionally resistant to deformation. As a result of these hybrid bonding characteristics, all ten 3d TMCs are mechanically stable in the RS structure.

To further investigate stability, we calculated the phonon dispersion curves of all 3d TMCs. As summarized in Table 1, we identify seven compounds as dynamically stable in the ZB structure, five in the RS structure, and zero in the CsCl structure. The presence of imaginary frequencies, as shown in Fig. S2 of the Supplementary Material, shows the dynamical instability of all the carbides in CsCl structure. The persistent instability of TMCs in the densely packed CsCl structure arises from its 8-fold coordination, which is deleterious to covalently bound systems such as the carbides studied here. The CsCl structure, with an 8-fold coordination, is commonly adopted by ionic systems as it maximizes (minimizes) the electrostatic attraction (distance) between cations and anions with a radius mismatch ratio near 0.64, according to Pauling's rules. In addition, an 8-fold coordination with square antiprismatic geometry would require sp^3d^4 hybridization, which is rare owing to its high energy cost [101,102]. Indeed, previous works have demonstrated that TMCs may adopt the CsCl structure only at exceptionally high pressures, coupled with a transition to metallic bonding [103,104]. As we aim to focus only on materials which may be useful under ambient conditions, we exclude the CsCl structure from consideration for the remainder of this work. With respect to the RS and ZB structures, our calculations confirm the stability of the previously reported TMCs based on the early transition metals (e.g., ScC, TiC, VC, and CrC) [100]. Purely predictive findings are proposed for the intermediate and late TMCs.

To uncover the origin of instability throughout intermediate TMCs in the RS and ZB structures, we identify any regions of the Brillouin zone in which phonon modes exhibit imaginary frequencies. Intermediate TMCs in the RS structure are found to exhibit instabilities surrounding the L point, with $\vec{k} = \frac{2\pi}{a}(0.5, 0.5, 0.5)$. As illustrated for MnC in Fig. 1, the associated phonon mode yields an off-center displacement of the central transition metal atom toward an edge of the octahedral complex, therefore shortening the 2nd nearest-neighbor metal-metal bond. Specifically, the energy of the system is minimized when the separation between adjacent metal atoms is equal to 2.605 Å, reflecting the formation of Mn^{4+} dimers [105]. From an orbital occupation perspective, this effect can be related to the nominal d^1 configuration which Mn adopts owing to the tetravalent state of the carbides. Each metal ion contributes one electron to the metal-metal bond, therefore forming an energetically

Table 1

Calculated volumes (V), normalized per formula unit (f.u.), for all 3d transition metal carbides (TMCs) in the zincblende, rocksalt, and cesium chloride structures. Previously computed data, where available, are given for comparison. The mechanical and dynamical stability of each compound are also presented. "MS/MU" correspond to the mechanically stable/unstable according to the Born criteria and "DS/DU" correspond to the dynamically stable/unstable as indicated by fully real-valued phonon mode frequencies.

| Compound	Zincblende		Rocksalt		Cesium chloride	
	V (Å^3/f.u.)	Stability	V (Å^3/f.u.)	Stability	V (Å^3/f.u.)	Stability
ScC	32.78	MU, DU	25.71 25.72[T,a]	MS, DS	23.81	MU, DU
TiC	26.50	MS, DS	20.40 20.37[T,a]	MS, DS	19.97	MU, DU
VC	23.04	MS, DS	18.08 18.03[T,a]	MS, DS	17.51	MU, DU
CrC	21.14	MS, DS	16.91 16.96[T,b]	MS, DS	16.12	MS, DU
MnC	20.06	MS, DS	16.31	MS, DU	15.33	MS, DU
FeC	19.27	MS, DS	15.95	MS, DU	15.00	MU, DU
CoC	19.50	MS, DS	16.14	MS, DU	15.48	MU, DU
NiC	20.60	MS, DU	16.82[T,a] 16.95	MS, DU	16.35	MU, DU
CuC	22.72	MU, DU	18.95	MS, DU	18.44	MU, DU
ZnC	25.72	MS, DS	21.31	MS, DS	21.06	MU, DU

[a] Ref. [92].
[b] Ref. [94].
[T] Computed value.
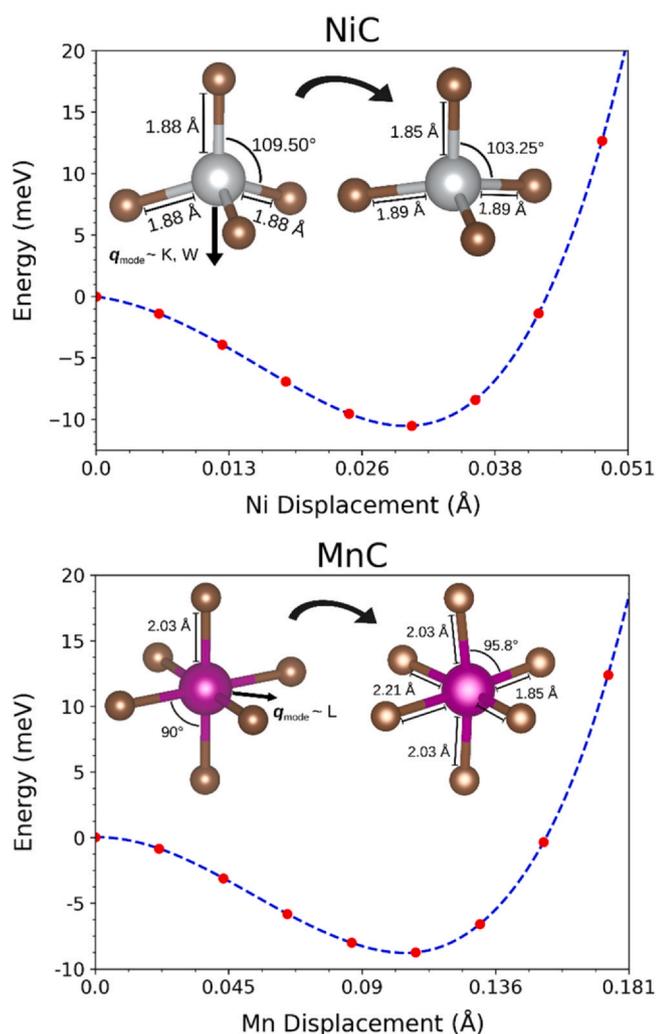
Fig. 1. Illustration of the energy landscapes, modulated along instabilities at high-symmetry points according to phonon dispersion calculations, for NiC (top) and MnC (bottom) in the zincblende and rocksalt structures respectively. Insets show local bonding configurations (tetrahedra and octahedra) before and after application of distortions. For the latter, bond lengths and angles corresponding to a minimum in energy are listed.

preferred singlet state. Based on our calculated maps of the electron localization function (i.e., ELF maps displayed in Fig. S9 of the Supplementary Material), the metal-metal interactions are mostly metallic in nature as electrons are delocalized between adjacent metal atoms with low ELF values (< 0.5) [106]. The effects of metallic dimerization are further illustrated by the projected electronic density of states displayed in Fig. 2. While the early TMCs exhibit complete occupation of the hybridized p-e_g orbitals and little to no occupation of the higher-energy p-t_{2g} orbitals, the latter frontiers display increasing occupation as the electron count is raised throughout the intermediate TMCs, including MnC and NiC. Since the apices of the t_{2g} orbitals lie directly between metal-carbon bonds within the octahedral coordination, they show some degree of overlap between the 2nd-nearest neighbor metal atoms. As a result, the initially non-bonding electrons occupying the t_{2g} orbitals begin to interact with one another, encouraging the formation of metal dimers. Moreover, the distortions associated with dimerization face only weak resistance from the exceedingly weak metal-carbon bonds found in the intermediate TMCs, as will be discussed in Section 3.2. These combined effects of increased metal-metal interactions and decreased metal-carbon strengths yield the dynamic instabilities found in the RS configurations of MnC, FeC, CoC, NiC, and CuC.

For compounds adopting the ZB structure, the origin of instability can be divided into two major categories: those occurring in ScC, an early TMC, and those occurring in the intermediate-to-late TMCs of Ni and Cu. The former case of ScC is characterized solely by elastic instabilities, as demonstrated by the aforementioned low value of C_{11} and equivalently the soft acoustic phonons surrounding the Γ zone-center shown in Fig. S3 of the Supplementary Material. In addition to the effects of connectivity and density discussed earlier in this Section, the instability of ScC can also be attributed to its unsaturated metal-carbon bonds, given that Sc may only contribute three valence electrons per atom. In contrast to the CsCl and RS structures, wherein respective metallic and ionic interactions may play a significant role, the ZB configuration relies heavily on covalent bonding. These bonds are insufficiently supported by the partially occupied orbitals in ScC, and therefore its structure is unstable with respect to cell distortions. In contrast, there is an excess of valence electrons available to participate in covalent bonding for both NiC and CuC, with nominal configurations of d^6 and d^7 respectively. Further distinguishing from ScC, these intermediate TMCs are prone to dynamic instabilities associated with imaginary phonon

Zincblende Structure
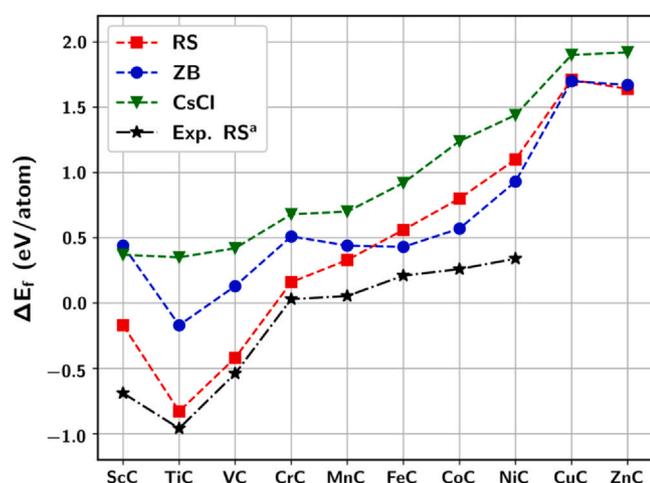

Rocksalt Structure
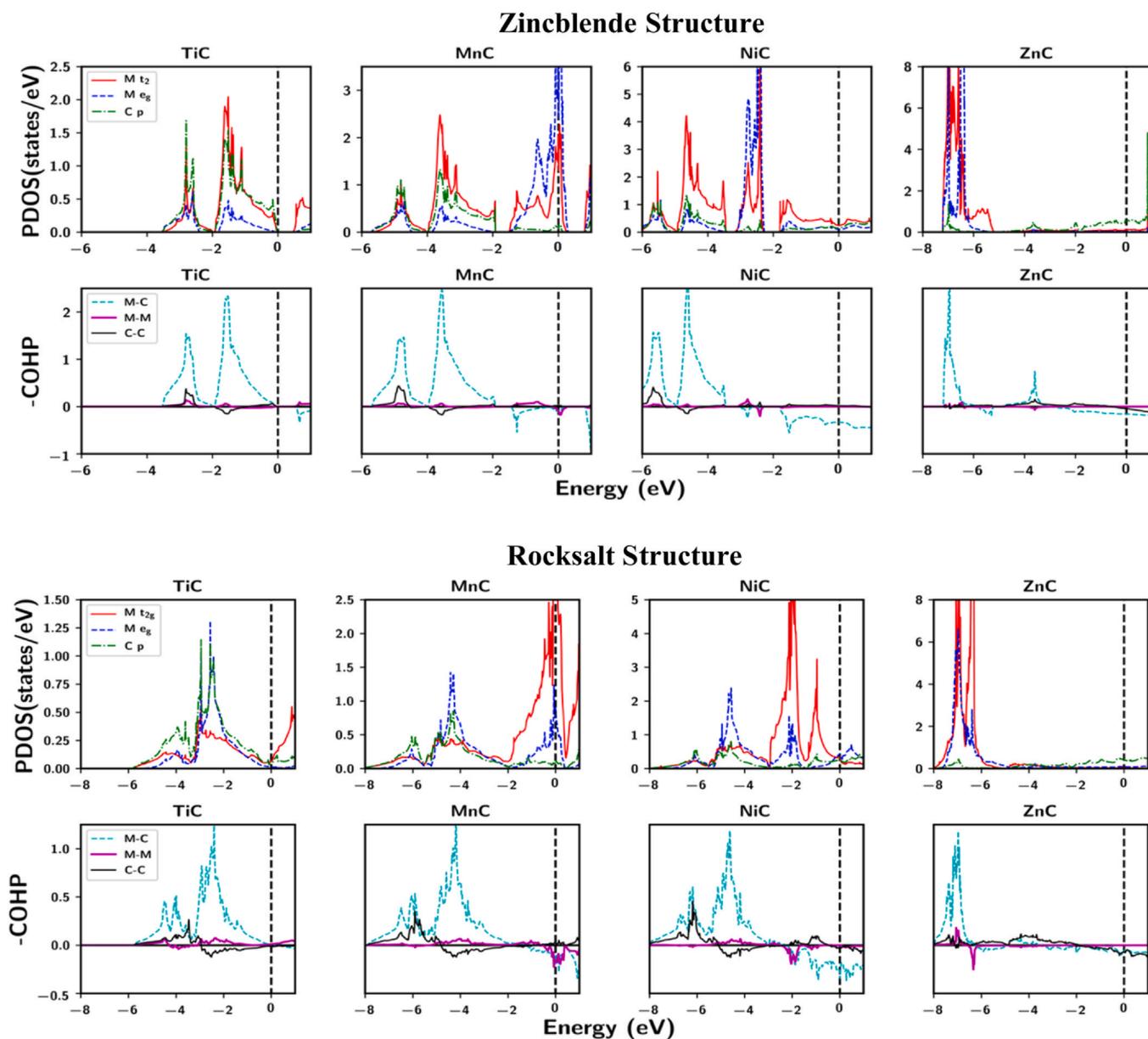
Fig. 2. Projected density of states (PDOS) and Crystal Orbital Hamiltonian Populations (COHP) of four unique TMCs spanning the 3d row. Compounds considered in the zincblende and rocksalt [113] structures are presented in the top and bottom panels respectively. For the PDOS, 3d densities are separated into t_{2g} and e_g components to illustrate the effects of crystal field splitting. In the COHP curves, covalent interactions among metal-carbon (M−C), metal-metal (M−M), and carbon-carbon (C−C) bonding pairs are shown. Positive and negative values of COHP represent bonding and antibonding respectively. For all plots, the Fermi energy is set to 0 eV.

frequencies surrounding the K and W points of the Brillouin zone, with coordinates of $\vec{k} = \frac{2\pi}{a}(0.75, 0.75, 0.0)$ and $\vec{k} = \frac{2\pi}{a}(0.5, 1.0, 0.0)$ respectively. By following the corresponding atomic displacements, we identify an off-center displacement of the central metal atom parallel and away from the direction of one of the coordinated carbon atoms, essentially flattening the tetrahedral complex. This effect, illustrated for NiC in Fig. 1, leads to a decrease in energy of 10 meV when the nickel atom is displaced by about 0.03 Å. The distortions found in NiC and CuC are suggestive of a Jahn-Teller instability [57–59]. In the tetrahedral ligand field of the ZB structure, the 3d orbitals are split into two low-energy e orbitals and three high-energy t_2 orbitals. When t_2 orbitals become sufficiently occupied, as in the d^6 configuration of NiC, there are three degenerate electron configurations possible. By Jahn-Teller distorting (i.e., by displacing the central atom and lowering the symmetry of the tetrahedral ligand field), a lower-energy configuration is adopted. This

is further supported by the projected electron density of states, shown for NiC in Fig. 2, which display partially occupied, non-bonding t_2 orbitals near the Fermi level. These states are initially degenerate and high-energy in the ideal tetrahedral coordination. However, as the orbitals are only partially filled by the d^6 configuration of NiC, the total energy of the system can be decreased via the aforementioned displacement of the central metal atom, which serves to enhance hybridization between the t_2 and p orbitals of the three nearest carbon atoms. Accordingly, both NiC and CuC are unstable in the ZB structure, whereas earlier TMCs may retain their ideal tetrahedral geometries owing to their decreased electron count serving to mitigate the incentive for Jahn-Teller [59,107] distortions.

Lastly, we study the thermodynamic stability of the TMCs in each structure by calculating the formation energy with respect to the constituent elements in their ground states, with results displayed in Fig. 3. Agreeing with their previously discussed dynamic instability in the earlier paragraph, all compounds adopting the CsCl structure

Fig. 3. Calculated formation energies of all 3d transition metal carbides in the rocksalt structure (RS), zincblende structure (ZB), and cesium chloride structures (CsCl). Symbols represent calculated values, whereas the lines represent interpolations plotted to highlight general trends. (a): Experimental formation energies are from Ref. [40].

are highly unstable with respect to decomposition, as signified by large, positive formation energies. In contrast, compounds in the RS and ZB structures generally exhibit much lower formation energies than those in the CsCl structure. Between these two configurations, RS is preferred for earlier TMCs owing to the substantial ionic character of their bonds, whereas ZB becomes energetically favorable for intermediate to late TMCs for which covalent interactions play a greater role. We emphasize that the vast majority of TMCs, regardless of structure, are thermodynamically unstable – agreeing with previous reports in the literature suggesting the difficulty to synthesize a variety of crystalline, stoichiometric carbides containing elements beyond Ti and Cr [40,46]. Indeed, the calculated stability and experimental synthesizability of TMCs are both restricted to the early transition metals. ScC, TiC, and VC are thermodynamically stable and experimentally synthesizable [108–110]. Although CrC is thermodynamically unstable, its formation energy is relatively low, and it can be accessed using low-temperature synthesis techniques [111].

Trends in formation energy across the period can be directly correlated with the effects d orbital filling, which influence the occupation of bonding and anti-bonding states. To more clearly illustrate this effect, we analyze the COHP curves displayed in Fig. 2 wherein positive values (above the y-axis) and negative values (below the y-axis) represent bonding and anti-bonding interactions respectively. First, ScC is shown to contain only partially filled bonding states resulting from the inability of Sc (s^2d^1) to contribute four electrons to its metal-carbon bonds. Despite this shortcoming, its high ionicity yields negative formation energies in the RS and ZB structures. Next, the increase in electron count allows all metal-carbon bonds to saturate as reflected by completely filled bonding states in the COHP curves. For this reason, TiC displays the lowest negative formation energy out of all TMCs studied here. From TiC on to the intermediate and late TMCs, the increasing electron count causes the antibonding states to become partially filled. These unfavorable interactions, mediated by electron repulsion, cause the formation energies to continuously increase moving from left to right across the period.

Subtle deviations from the monotonic trend in formation energy described above are observed in TMCs where magnetic ordering plays a significant role. Both MnC and FeC adopt a ferromagnetic ground state caused by a Stoner instability [112] in which the intra-atomic exchange and electronic occupation at the Fermi level

become sufficiently strong such that ferromagnetic ordering is preferred. The ferromagnetic rearrangement of electrons allows the majority-spin M-M bonding states to become fully occupied (fall below the Fermi level), while the minority-spin M-M antibonding states become unoccupied (rise above the Fermi level). This is illustrated by our spin-polarized COHP plots provided in Fig. S8 of the Supplementary Material. A more in-depth analysis of ferromagnetic instabilities in RS TMCs can be found in our previous work [113].

Lastly, ZnC acts independently owing to its filled, nonbonding d shell, resulting in a slightly lower formation energy than the carbides of nearby metals. Because Zn has no unpaired electrons, it is more electropositive than nearby metals – e.g., Zn has an electronegativity of 1.66, whereas Cu has an electronegativity of 1.75 [114]. Therefore, the ionic contribution to the metal-carbon bonding is greater in ZnC than in TMCs with a comparable (lower) atomic number. Despite this difference, ZnC remains highly thermodynamically unstable, with an energy of 1.64 eV/atom above the convex hull formed by Zn and C.

As mentioned previously, we chose to focus on cubic structures as they are suspected to have promising mechanical properties. However, for the sake of completeness in our analysis, we also tested all ten TMCs in the hexagonal (wurtzite) structure, with the corresponding formation energies listed in Table S6 of the Supplementary Material. The results indicate the a hexagonal structure is preferred only for CrC and MnC. However, these still remain unstable with respect to decomposition into elemental ground states. We note that while most of the intermediate and late TMCs are thermodynamically unstable, many of those identified as dynamically stable may still be synthesizable using chimie douce techniques, which are commonly employed to access metastable states.

3.2. Bonding and mechanical properties

To study the mechanical properties, we look to the calculated elastic constants displayed in Fig. 4 and provide an explanation of any trends throughout the TMCs by analyzing their electronic structure. From the elastic constants, derived quantities including bulk moduli, shear moduli, Vicker's hardness, Cauchy's pressure, Poisson's ration and Pugh's ratio are listed in Table S2 of the Supplementary Material, and are in good agreement with available experimental [115,116] and calculated [33] values. The derived quantities such as bulk moduli, shear moduli, and Vicker's hardness are displayed in Fig. 5 to gain insight into directly observable properties. For both the ZB and RS structures, we find that increasing valence electron concentrations leads to higher values of C_{11} and C_{12} throughout many of the stable TMCs. These changes raise the bulk moduli across the intermediate TMCs, with maxima occurring at FeC and CrC in ZB and RS respectively, corresponding to calculated bulk moduli of 252.9 GPa and 326.4 GPa.

The observed correlation between bulk modulus and group number can be attributed to three effects. First, the introduction of additional valence electrons (beyond a configuration of d^0 in TiC) mediates increased filling of the antibonding states. In this respect, the PDOS plots in Fig. 2 illustrate that the Fermi level monotonically increases moving left to right across the periodic table, leading to enhanced occupation of the high-lying t_2 and e_g states in the ZB and RS structures respectively. From the COHP curves, these states are confirmed to be strongly antibonding in nature. Consequently, a higher occupation of the antibonding orbitals ensures that the structures are more resistant to compression given that such deformation will decrease the metal-carbon bond lengths and therefore raise the energy of the antibonding levels [117,118]. The changing occupation of the antibonding orbitals are quantified by integrating COHP curves below the Fermi level, yielding ipCOHP values whereby larger (more positive) values signify enhanced bonding and decreased antibonding. As shown in Table S7 in
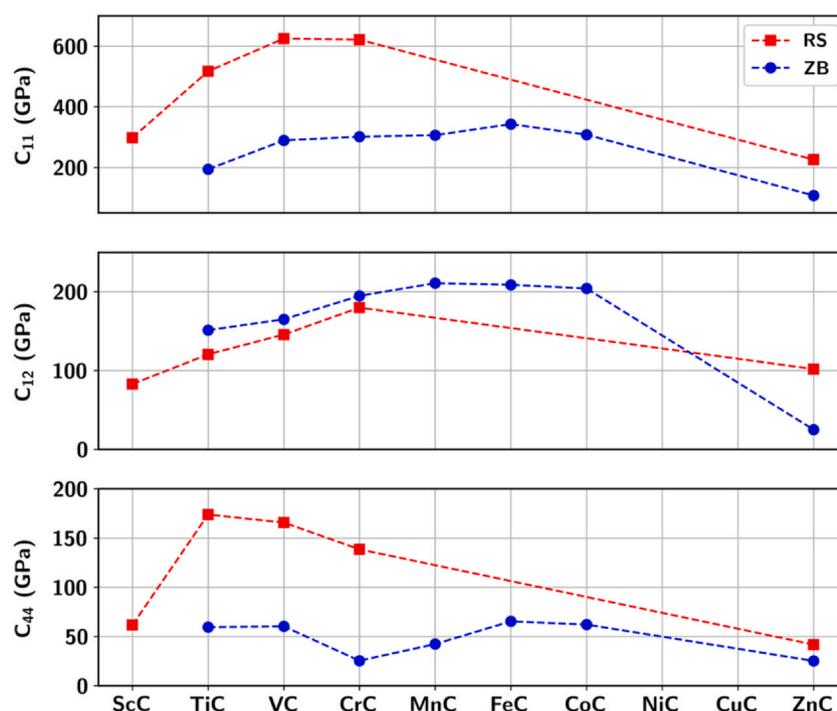
Fig. 4. Independent elastic constants (C_{11}, C_{12}, C_{44}) shown for all the stable/metastable compounds in the rocksalt structure (RS) and zincblende structure (ZB). Symbols represent calculated values, whereas the lines represent interpolations plotted to highlight general trends.

Supplemental Material, a maximum ipCOHP is achieved for TiC in both structures (2.23 eV and 1.55 eV for ZB and RS, respectively), whereas ipCOHP decreases across the later TMCs as the covalent interaction strength weakens. Second, the amount of electronic charge transferred between the metal and the carbon ions varies with the electronegativity of the TM. These changes, quantified by our Bader charge transfer values listed in Table S4 of the Supplemental Material, show that less charge is transferred between the

ions in the late TMCs. Those TMCs with lower charge transfer tend to have higher bulk moduli as their attractive electrostatic force is decreased – hence, compression is favored less. Third, intermediate TMCs adopt structures with higher atomic densities owing to their short ionic radii. The increased strength of electrostatic repulsions acting across shorter distances encourages a more robust resistance to compression and therefore higher bulk moduli. In contrast, both electronic and steric effects lead to lower values of C_{11} and C_{12} in the
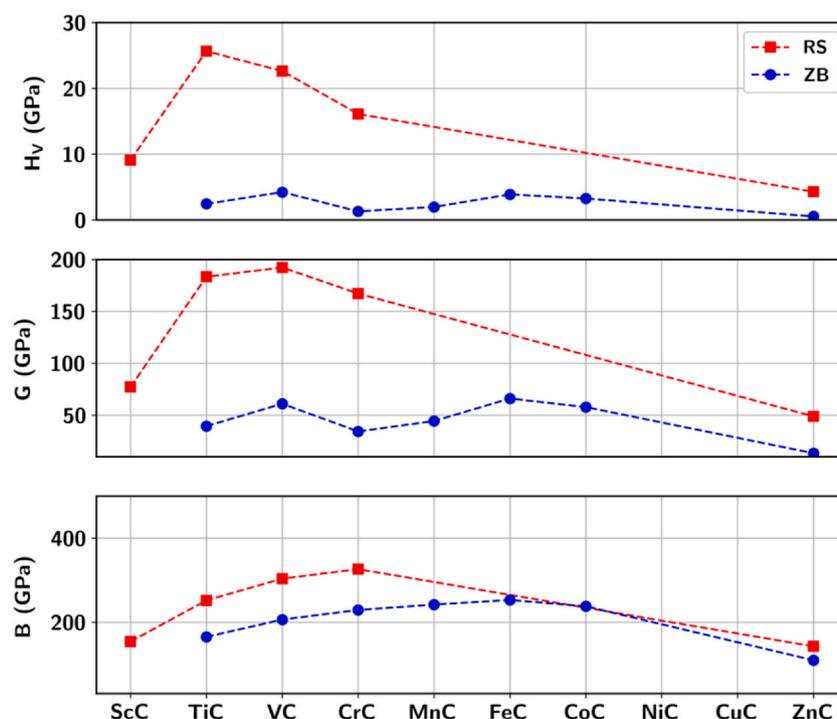
Fig. 5. Correlation of Vickers hardness (H_V), shear modulus (G), and bulk modulus (B) with increasing group number across all stable/metastable 3d TMCs in the rocksalt structure (RS) and zincblende structure (ZB). Symbols represent calculated values, whereas the lines represent interpolations plotted to highlight general trends.

late TMCs. ZnC, for example, has a filled d shell in which many of its valence electrons occupy non-bonding states as confirmed by the COHP curves shown in Fig. 2. The corresponding orbitals respond weakly to compression, thus contributing little to the mechanical properties. Moreover, the atomic density of ZnC is relatively low, further reducing its bulk modulus.

There appears to be a more subtle relationship between C_{44} and group number across the TMCs that correlate quite closely with the calculated formation energies. Initially, C_{44} exhibits a large increase from ScC to TiC owing to a complete filling of the bonding orbitals as shown in the PDOS and COHP curves. For RS-structured compounds beyond TiC, a clear monotonic decrease in C_{44} is observed with increasing group number due to enhanced filling of the antibonding orbitals. Electrons occupying these states favor shearing as it reduces overlap between σ orbitals mediating nearest-neighbor bonds in the RS structure, thereby lowering the energy of the antibonding levels. Moreover, an increased electron count favors shearing as it enhances d orbital overlap between TM neighbors, thereby enabling metal dimer formation as discussed in the previous section. This further contributes to low values of C_{44} in the intermediate-late TMCs. Interestingly, changes in C_{44} are somewhat different for TMCs adopting the ZB structure. In this case, C_{44} displays a minimum for CrC before increasing back to relatively high values across the intermediate TMCs with a maximum at FeC. Then, a return back to low C_{44} is shown for the late TMCs such as ZnC. We propose that magnetic ordering likely plays a large role in lowering the occupation of antibonding states in the intermediate TMCs, as the splitting of majority- and minority-spin states reduces Pauli repulsion between like electrons. Similar trends may indeed be observed throughout compounds in the RS structure. However, most intermediate TMCs are not stable in this structure and therefore cannot be reliably considered.

To further investigate the effect of structure on the resulting mechanical properties, we directly compare the elastic constants calculated for each compound adopting RS and ZB structures. Fig. 4 shows that C_{11} and C_{44} are consistently larger in the RS structure, C_{12} is more dominant in ZB. These differences arise from the underlying bonding configurations of each structure, as the direct σ overlap between metal d and carbon p orbitals in the RS structure ensure is highly resistant to uniaxial compression (C_{11}) and shearing (C_{44}). However, this same configuration is relatively dense and displays weaker resistance to transverse strain (C_{12}). In contrast, direct σ-bonding in the ZB structures requires some energy cost associated with hybridization as the original (atomic) d orbitals do not directly overlap with the carbon p orbitals. Furthermore, the tetrahedral coordination environments comprising the ZB structure are more readily distorted without causing substantial compression or elongation of individual bond lengths. These features lower the observed values of C_{11} and shearing C_{44}. Though, because compounds adopting the ZB structure have larger volumes, they readily accommodate volume dilation associated with higher values of C_{12}.

Differences in atomic interactions can also be illustrated through analysis of the phonon dispersion curves, which are plotted for TiC and ZnC in Fig. 6. Between RS and ZB structures, there are several key distinguishing features. First, the slope of the acoustic branch near the Γ point is higher in the RS structure for the early TMCs (as shown by TiC), which suggests increased hardness and is in good agreement with our calculated elastic constants. In contrast, ZnC has very soft (low-frequency and weakly sloped) acoustic phonon modes near Γ when adopting the RS structure, which reflects weaker metal-carbon bonding due to the filled 3d states as supported by our earlier COHP analysis. On the other hand, increased covalent interactions in the ZB structure stabilize a raised slope in the acoustic branches near Γ for ZnC. Second, while the RS phonon dispersion curves display large anomalies (e.g., deviations in the longitudinal acoustic mode along Γ-X) that indicate strong electron-phonon coupling, in
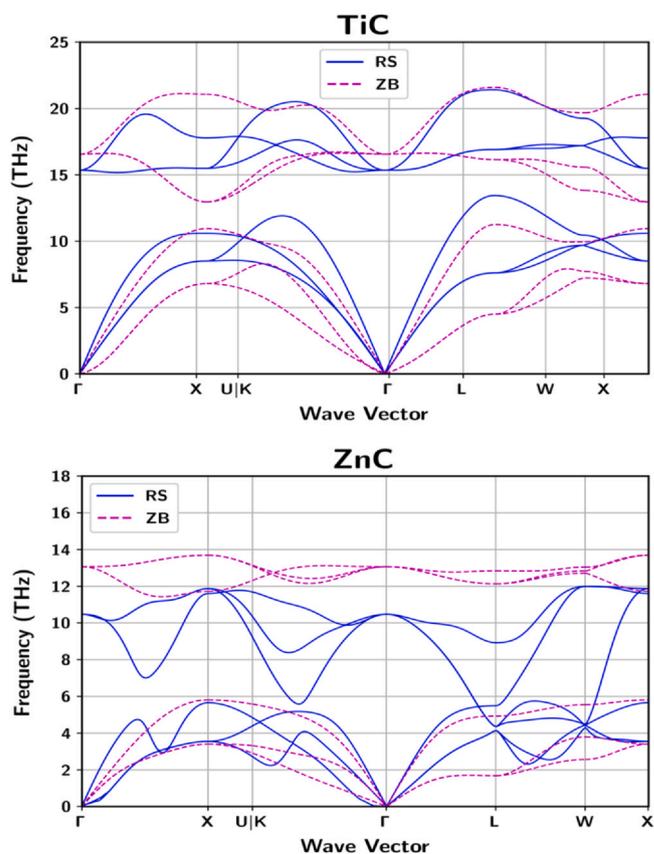

Fig. 6. Phonon dispersion curves for TiC and ZnC, each of which represents extrema in the valence electron concentration of all stable compounds. To illustrate dynamic differences arising from varying structural factors, individual curves are plotted for the rocksalt (RS) and zincblende (ZB) structures.

accordance with previous work [113], the ZB phonon dispersion curves display no noticeable anomalies. This highlights the difference in local interactions between metal d orbitals; electron-phonon coupling in RS is mediated by significant d-d overlap between nearest metal neighbors, whereas the distance between metal atoms in the ZB structure is too large to support any significant coupling via d-d interactions. Hence, unconventional superconductivity is suspected in the RS structure, but not in the ZB structure. Last, the optical frequencies of the ZB structure are shown to be higher than those in the RS structure for TiC and ZnC, possibly due to enhanced C-C interactions [119]. Despite the longer C−C bond lengths in the ZB structure relative to the RS structure, the tetrahedral coordination of the ZB structure is suspected to mediate stronger overlap of the *p* orbitals when compared to the octahedral coordination of the RS structure. This is supported by our calculated ipCOHP values, which show enhanced C-C interaction in the ZB structure (80 meV) relative to the RS structure (30 meV) for TiC. Interestingly, despite the increased mass mismatch between Zn and C (as opposed to Ti and C), significant acoustic/optical overlap is observed in RS-structured ZnC, further signifying the anomalous behavior of that compound due to its filled d shell and strong electron-phonon coupling.

Last, to consider these TMCs as applications in hard coatings, it is of interest to determine their hardness (measured by Vicker's hardness) and ductility. A material is expected to be ductile if its Pugh's ratio is below 0.5–0.6, its Poisson's ratio is above 0.25–0.28, and its Cauchy pressure is greater than zero [120]. Here, we find that TMCs maintain much higher values of Vicker's hardness in the RS structure as opposed to ZB. This difference can be traced back to the lower values of C_{44} found in the ZB structure as discussed in the previous paragraph, which preclude them from being used for high-

Table 2

Calculated Cauchy's pressure (P_c), Poisson's ratio (ν), and Pugh's ratio (κ) of each stable 3d transition metal carbides (TMCs) in the zincblende structure (ZB) and rocksalt structure (RS). Instability is denoted by "U". Since all TMCs are unstable in the cesium chloride structure (CsCl), the corresponding values are not presented here.

TMCs	$P_{c \ (GPa)}$		ν		κ	
	ZB	RS	ZB	RS	ZB	RS
ScC	U	21.4	U	0.29	U	0.50
TiC	91.6	- 53.5	0.39	0.21	0.24	0.73
VC	104.7	- 20.1	0.37	0.24	0.30	0.63
CrC	167.3	41.2	0.43	0.28	0.15	0.51
MnC	168.5	U	0.41	U	0.18	U
FeC	143.4	U	0.38	U	0.26	U
CoC	141.9	U	0.39	U	0.24	U
ZnC	82.1	60.2	0.44	0.35	0.12	0.34

hardness coating applications. As for the RS materials, a maximum hardness of 25.66 GPa is identified in TiC, matching with previous findings [121]. Though, both VC and CrC also display reasonably high hardnesses of 22.63 and 16.11 GPa respectively. Of these compounds, both TiC and VC are predicted to be brittle according to their reported values of Pugh's ratios, Poisson's ratios, and Cauchy pressures in Table 2. For the remaining stable TMCs, their properties instead show ductile behavior. Therefore, although TiC is the hardest material studied here, we propose that CrC may be preferred in applications where toughness is also required.

4. Conclusion

In summary, our work illustrates how valence electron concentration and structure play dominant roles in controlling the stability and mechanical performance of 3d TMCs. Across early TMCs adopting the RS structure, comprising the most widely studied systems, our findings confirm the importance of filled bonding states to enable robust stability and exceptionally high hardness. Furthermore, we build upon existing understanding to provide novel insight into the source of instability of the RS structure throughout the intermediate TMCs, which is shown to correlate with enhanced metal-metal interactions and weakened metal-carbon bonds. With regards to the ZB structure, our calculations reveal several new compounds that are metastable and potentially synthesizable if the thermodynamic ground state can be avoided (e.g., via chimie douce techniques). Although their mechanical properties are not as promising as those displayed by TMCs in the RS structure, they may warrant further investigation considering the possibility of potentially interesting and unexpected electronic properties. Lastly considering the CsCl structure, we predict that all 3d TMCs are unstable under ambient conditions owing to the dense eight-fold coordination that constitutes the local bonding environments in CsCl and that does not accommodate the highly covalent bonding in the carbides. Though, high-pressure studies may be worthwhile to investigate whether stabilization can be obtained through many of the TMCs. If this can be accomplished, there exists a possibility to find new and interesting properties such as unconventional superconductivity previously reported [113] in several RS TMCs.

Based on the findings presented above, we focus on the RS structure and propose several guiding principles for the design of novel TMCs that may be used in next-generation hard coating applications. First, to maximize hardness and stability, a valence electron count of four (e.g., TiC) is critical. In this case, covalent M-C interactions dominate owing to the completely filled bonding orbitals, whereas metallic M-M interactions are minimized because of the d^0 configuration (empty metal orbitals). Second, if ductility rather than hardness is to be optimized, then a valence electron count well beyond four is favorable. In this case, M-M interactions play a larger role as the non-bonding d orbitals become filled, which favor

shearing deformations that allow the d orbitals to overlap. However, it is also important to prevent over-filling of the d orbitals so that the structure does not become dynamically unstable with respect to metal dimer formation (e.g., as in MnC). Third, to achieve tough materials with a balance between hardness and ductility, one may consider a valence electron count that is only slightly higher than four. Because an increase beyond four electrons causes enhanced ductility but worsened hardness, we suggest that an optimal tradeoff may be realized through ion substitution – e.g., between TiC and CrC. By forming solid solutions with controllable compositions, the mechanical properties may be fine-tuned by varying Ti-Cr content. Although past works suggest that high temperatures are necessary to form such solutions [122], alternative techniques such as high-energy ball milling or doping (e.g., high-entropy alloys) may be considered in the future.

CRediT authorship contribution statement

Indiras Khatri: Conceptualization (Lead), Formal analysis (Lead), Methodology (Lead), Software (Lead), Writing – original draft (Lead). **Nathan J. Szymanski:** Conceptualization (Equal), Investigating (Equal), Validation (Lead), Writing – review & editing (Equal). **Bishal Babu Dumre:** Methodology (Supporting). **Jacques G. Amar:** Funding acquisition (Lead), Project administration (Lead), Validation (Lead), Writing – review & editing: Supporting). **Daniel Gall:** Validation (Supporting), Writing – review & editing (Supporting). **Sanjay V. Khare:** Conceptualization (Supporting), Funding acquisition (Lead), Project administration (Lead), Writing – review & editing (Supporting).

Declaration of Competing Interest

The authors declare that they have no known competing financial interests or personal relationships that could have appeared to influence the work reported in this paper.

Acknowledgements

Disclaimer

The views and conclusions contained herein are those of the authors and should not be interpreted as necessarily representing the official policies or endorsements, either expressed or implied, of Air Force Research Laboratory or the U.S. Government.

Appendix A. Supporting information

Supplementary data associated with this article can be found in the online version at doi:10.1016/j.jallcom.2021.161866.

References

[1] L.E. Toth, Transition Metal Carbides and Nitrides, Elsevier, 2014.
[2] C. Kral, W. Lengauer, D. Rafaja, P. Ettmayer, Critical review on the elastic properties of transition metal carbides, nitrides and carbonitrides, J. Alloy. Compd. 265 (1998) 215–233.

[3] X. Zhou, D. Gall, S.V. Khare, Mechanical properties and electronic structure of anti-ReO3 structured cubic nitrides, M₃N, of d block transition metals M: an ab initio study, J. Alloy. Compd. 595 (2014) 80–86.

[4] J.G. Chen, J. Eng Jr., S. Kelty, NEXAFS determination of electronic and catalytic properties of transition metal carbides and nitrides: from single crystal surfaces to powder catalysts, Catal. Today 43 (1998) 147–158.

[5] S. Kodambaka, S.V. Khare, W. Swiech, K. Ohmori, I. Petrov, J.E. Greene, Dislocation-driven surface dynamics on solids, Nature 429 (2004) 49–52.

[6] H.H. Hwu, J.G. Chen, Surface chemistry of transition metal carbides, Chem. Rev. 105 (2005) 185–212.

[7] S. Kodambaka, S.V. Khare, V. Petrova, D.D. Johnson, I. Petrov, J.E. Greene, Absolute orientation-dependent anisotropic TiN (111) island step energies and stiffnesses from shape fluctuation analyses, Phys. Rev. B 67 (2003) 035409.

[8] L.I. Johansson, Electronic and structural properties of transition-metal carbide and nitride surfaces, Surf. Sci. Rep. 21 (1995) 177–250.

[9] H. Li, L. Zhang, Q. Zeng, K. Guan, K. Li, H. Ren, S. Liu, L. Cheng, Structural, elastic and electronic properties of transition metal carbides TMC (TM= Ti, Zr, Hf and Ta) from first-principles calculations, Solid State Commun. 151 (2011) 602–606.

[10] K. Zhang, K. Balasubramanian, B.D. Ozsdolay, C.P. Mulligan, S.V. Khare, W.T. Zheng, D. Gall, Growth and mechanical properties of epitaxial NbN (001) films on MgO (001), Surf. Coat. Technol. 288 (2016) 105–114.

[11] J. Häglund, G. Grimvall, T. Jarlborg, A.F. Guillermet, Band structure and cohesive properties of 3d-transition-metal carbides and nitrides with the NaCl-type structure, Phys. Rev. B Condens Matter 43 (1991) 14400–14408.

[12] S. Kodambaka, V. Petrova, S.V. Khare, D. Gall, A. Rockett, I. Petrov, J.E. Greene, Size-dependent detachment-limited decay kinetics of two-dimensional TiN islands on TiN (111), Phys. Rev. Lett. 89 (2002) 176102.

[13] N. Koutná, A. Brenner, D. Holec, P.H. Mayrhofer, High-throughput first-principles search for ceramic superlattices with improved ductility and fracture resistance, Acta Mater. 206 (2021) 116615.

[14] K. Balasubramanian, S.V. Khare, D. Gall, Energetics of point defects in rocksalt structure transition metal nitrides: thermodynamic reasons for deviations from stoichiometry, Acta Mater. 159 (2018) 77–88.

[15] F. Benesovsky, R. Kieffer, P. Ettmayer, Nitrides, Encycl. Chem. Technol. 15 (1981) 871–881.

[16] R. Levy, M. Boudart, Platinum-like behavior of tungsten carbide in surface catalysis, Science 181 (1973) 547–549.

[17] S.T. Oyama, Preparation and catalytic properties of transition metal carbides and nitrides, Catal. Today 15 (1992) 179–200.

[18] S.T. Oyama, Introduction to the Chemistry of Transition Metal Carbides and Nitrides, in the Chemistry of Transition Metal Carbides and Nitrides, Springer, 1996, pp. 1–27.

[19] J.A. Warner, S. Patil, S.V. Khare, K.C. Masiulaniec, Ab initio calculations for properties of MAX phases Ti₂TlC, Zr₂TlC, and Hf₂TlC, Appl. Phys. Lett. 88 (2006) 101911.

[20] S.K.R. Patil, N.S. Mangale, S.V. Khare, S. Marsillac, Super hard cubic phases of period VI transition metal nitrides: First principles investigation, Thin Solid Films 517 (2008) 824–827.

[21] L.L. Wang, S.V. Khare, V. Chirita, D.D. Johnson, A.A. Rockett, A.I. Frenkel, N.H. Mack, R.G. Nuzzo, Origin of bulklike structure and bond length disorder of Pt₃₇ and Pt₆Ru₃₁ clusters on carbon: Comparison of theory and experiment, J. Am. Chem. Soc. 128 (2006) 131–142.

[22] B.D. Ozsdolay, C.P. Mulligan, K. Balasubramanian, L. Huang, S.V. Khare, D. Gall, Cubic β-WNx layers: growth and properties vs N-to-W ratio, Surf. Coat. Technol. 304 (2016) 98–107.

[23] S.V. Khare, T. Einstein, Energetics of steps and kinks on Ag and Pt using equivalent crystal theory (ECT), Surf. Sci. 314 (1994) L857–L865.

[24] J. Musil, Hard and superhard nanocomposite coatings, Surf. Coat. Technol. 125 (2000) 322–330.

[25] M. Yasuoka, P. Wang, R. Murakami, Comparison of the mechanical performance of cutting tools coated by either a TiCxN₁₋ₓ single-layer or a TiC/TiC₀.₅N₀.₅/TiN multilayer using the hollow cathode discharge ion plating method, Surf. Coat. Technol. 206 (2012) 2168–2172.

[26] Y. Zhong, X. Xia, F. Shi, J. Zhan, J. Tu, H.J. Fan, Transition metal carbides and nitrides in energy storage and conversion, Adv. Sci. 3 (2016) 1500286.

[27] B. Anasori, M.R. Lukatskaya, Y. Gogotsi, 2D metal carbides and nitrides (MXenes) for energy storage, Nat. Rev. Mater. 2 (2017) 1–17.

[28] M. Nagai, T. Kurakami, Reverse water gas shift reaction over molybdenum carbide, J. Chem. Eng. Jpn. 38 (2005) 807–812.

[29] R. Zhan, X. Luo, Topologically nontrivial phases in superconducting transition metal carbides, J. Appl. Phys. 125 (2019) 053903.

[30] A.F. Guillermet, J. Häglund, G. Grimvall, Cohesive properties of 4d-transition-metal carbides and nitrides in the NaCl-type structure, Phys. Rev. B 45 (1992) 11557–11567.

[31] K. Balasubramanian, S.V. Khare, D. Gall, Valence electron concentration as an indicator for mechanical properties in rocksalt structure nitrides, carbides and carbonitrides, Acta Mater. 152 (2018) 175–185.

[32] Z.T. Liu, X. Zhou, S.V. Khare, D. Gall, Structural, mechanical and electronic properties of 3d transition metal nitrides in cubic zincblende, rocksalt and cesium chloride structures: a first-principles investigation, J. Phys. Condens. Matter 26 (2014) 025404.

[33] L. Wu, T. Yao, Y. Wang, J. Zhang, F. Xiao, B. Liao, Understanding the mechanical properties of vanadium carbides: nano-indentation measurement and first-principles calculations, J. Alloy. Compd. 548 (2013) 60–64.

[34] D.D. Koelling, G.O. Arbman, Use of energy derivative of the radial solution in an augmented plane wave method: application to copper, J. Phys. F: Met. Phys. 5 (1975) 2041–2054.

[35] A.F. Guillermet, G. Grimvall, Cohesive properties and vibrational entropy of 3d transition-metal compounds, MX (NaCl) compounds (X= C, N, O, S), complex carbides, and nitrides, Phys. Rev. B Condens Matter 40 (1989) 10582–10593.

[36] J.E. Krzanowski, R.E. Leuchtner, Chemical, mechanical, and tribological properties of pulsed-laser-deposited titanium carbide and vanadium carbide, J. Am. Ceram. Soc. 80 (1997) 1277–1280.

[37] R. Ahuja, O. Eriksson, J.M. Wills, B. Johansson, Structural, elastic, and high-pressure properties of cubic TiC, TiN, and TiO, Phys. Rev. B Condens. Matter 53 (1996) 3072–3079.

[38] S.H. Cai, C.W. Liu, Studies on the band structures of some layered transition metal dichalcogenides, J. Mol. Struct. (Theochem.) 362 (1996) 379–385.

[39] J.L. Calais, Band structure of transition metal compounds, Adv. Phys. 26 (1977) 847–885.

[40] J. Häglund, A. Fernández Guillermet, G. Grimvall, M. Körling, Theory of bonding in transition-metal carbides and nitrides, Phys. Rev. B Condens. Matter 48 (1993) 11685–11691.

[41] A. Neckel, Recent investigations on the electronic structure of the fourth and fifth group transition metal monocarbides, mononitrides, and monoxides, Int. J. Quantum Chem. 23 (1983) 1317–1353.

[42] D.J. Singh, B.M. Klein, Electronic structure, lattice stability, and superconductivity of CrC, Phys. Rev. B Condens. Matter 46 (1992) 14969–14974.

[43] L. Benco, Metal-to-metal bonding in transition metal monocarbides and mononitrides, J. Solid State Chem. 128 (1997) 121–129.

[44] K.K. Korir, G.O. Amolo, N.W. Makau, D.P. Joubert, First-principle calculations of the bulk properties of 4d transition metal carbides and nitrides in the rocksalt, zincblende and wurtzite structures, Diam. Relat. Mater. 20 (2011) 157–164.

[45] C. Paduani, Electronic structure and Fermi surfaces of transition metal carbides with rocksalt structure, J. Phys.: Condens. Matter 20 (2008) 225014.

[46] M.G. Quesne, A. Roldan, N.H. de Leeuw, C. Catlow, Bulk and surface properties of metal carbides: implications for catalysis, Phys. Chem. Chem. Phys. 20 (2018) 6905–6916.

[47] Y. Zhang, J. Li, L. Zhou, S. Xiang, A theoretical study on the chemical bonding of 3d-transition-metal carbides, Solid State Commun. 121 (2002) 411–416.

[48] A. Vojvodic, C. Ruberto, Trends in bulk electron-structural features of rocksalt early transition-metal carbides, J. Phys. Condens. Matter 22 (2010) 375501.

[49] J. Maibam, B. Indrajit Sharma, R. Bhattacharjee, R.K. Thapa, R.K. Brojen Singh, Electronic structure and elastic properties of scandium carbide and yttrium carbide: a first principles study, Phys. B: Condens. Matter 406 (2011) 4041–4045.

[50] A.F. Guillermet, J. Häglund, G. Grimvall, Cohesive properties and electronic structure of 5d-transition-metal carbides and nitrides in the NaCl structure, Phys. Rev. B Condens. Matter 48 (1993) 11673–11684.

[51] J.C. Grossman, A. Mizel, M. Côté, M.L. Cohen, S.G. Louie, Transition metals and their carbides and nitrides: trends in electronic and structural properties, Phys. Rev. B 60 (1999) 6343–6347.

[52] Y.H. Zhao, H.Y. Su, K. Sun, J. Liu, W.X. Li, Structural and electronic properties of cobalt carbide Co₂C and its surface stability: density functional theory study, Surf. Sci. 606 (2012) 598–604.

[53] F. Viñes, C. Sousa, P. Liu, J.A. Rodriguez, F. Illas, A systematic density functional theory study of the electronic structure of bulk and (001) surface of transition-metals carbides, J. Chem. Phys. 122 (2005) 174709.

[54] Y. Yang, H. Lu, C. Yu, J.M. Chen, First-principles calculations of mechanical properties of TiC and TiN, J. Alloy. Compd. 485 (2009) 542–547.

[55] M. Fukuichi, First-Principles Calculations on the Origin of Mechanical Properties and Electronic Structures of 3d, 4d, and 5d Transitional Metal Monocarbides, Department of Physics, Osaka University, 2019. ⟨https://doi.org/10.18910/72647⟩.

[56] S.F. Pugh, Relations between the elastic moduli and the plastic properties of polycrystalline pure metals, Philos. Mag. (1954) 823–843.

[57] C.E. Housecroft, A.G. Sharpe, Chapter 22: d-block metal chemistry: the first row elements, Inorganic Chemistry, 716, 2008.

[58] M.A. Halcrow, Jahn–Teller distortions in transition metal compounds, and their importance in functional molecular and inorganic materials, Chem. Soc. Rev. (2013) 1784–1795.

[59] D. Reinen, M. Atanasov, G. Nikolov, F. Steffens, Localand cooperative Jahn-Teller distortions of nickel (2+) and copper (2+) intetrahedral coordination, Inorg. Chem. (1988) 1678–1686.

[60] G. Kresse, Ab initiomolecular-dynamics simulation of the liquid-metal–amorphous-semiconductor transition in germanium, Phys. Rev. B 49 (1994) 14251–14269.

[61] G. Kresse, J. Furthmüller, Efficiency of ab-initio total energy calculations for metals and semiconductors using a plane-wave basis set, Comput. Mater. Sci. 6 (1996) 15–50.

[62] G. Kresse, J. Hafner, Ab initio molecular dynamics for liquid metals, Phys. Rev. B Condens. Matter 47 (1993) 558–561.

[63] G. Kresse, J. Furthmüller, Efficient iterative schemes for ab initio total-energy calculations using a plane-wave basis set, Phys. Rev. B Condens. Matter 54 (1996) 11169–11186.

[64] P.E. Blöchl, Projector augmented-wave method, Phys. Rev. B Condens. Matter 50 (1994) 17953–17979.

[65] J.P. Perdew, K. Burke, M. Ernzerhof, Generalized gradient approximation made simple, Phys. Rev. Lett. 77 (1996) 3865–3868.

[66] H.J. Monkhorst, J.D. Pack, Special points for Brillouin-zone integrations, Phys. Rev. B 13 (1976) 5188–5192.

[67] J.D. Pack, H.J. Monkhorst, Special points for Brillouin-zone integrations—a reply, Phys. Rev. B 16 (1977) 1748–1749.

[68] B.B. Dumre, N.J. Szymanski, V. Adhikari, I. Khatri, D. Gall, S.V. Khare, Improved optoelectronic properties in $CdSe_xTe_{1-x}$ through controlled composition and short-range order, Sol. Energy 194 (2019) 742–750.

[69] B.B. Dumre, D. Gall, S.V. Khare, Stability, and electronic and optical properties of ternary nitride phases of $MgSnN_2$: a first-principles study, J. Phys. Chem. Solids 153 (2021) 110011.

[70] I. Efthimiopoulos, I. Khatri, Z. Liu, S.V. Khare, P. Sarin, V. Tsurkan, A. Loidl, D. Zhang, Y. Wang, Universal link of magnetic exchange and structural behavior under pressure in chromium spinels, Phys. Rev. B 97 (2018) 184435.

[71] I. Efthimiopoulos, Z. Liu, M. Kucway, S.V. Khare, P. Sarin, V. Tsurkan, A. Loidl, Y. Wang, Pressure-induced phase transitions in the $CdCr_2Se_4$ spinel, Phys. Rev. B 94 (2016) 174106.

[72] H. Fu, D. Li, F. Peng, T. Gao, X. Cheng, Ab initio calculations of elastic constants and thermodynamic properties of NiAl under high pressures, Comput. Mater. Sci. 44 (2008) 774–778.

[73] F. Murnaghan, The compressibility of media under extreme pressures, Proc. Natl. Acad. Sci. USA 30 (1944) 244–247.

[74] N.J. Szymanski, Z. Liu, T. Alderson, N.J. Podraza, P. Sarin, S.V. Khare, Electronic and optical properties of vanadium oxides from first principles, Comput. Mater. Sci. 146 (2018) 310–318.

[75] Z.T. Liu, B.P. Burton, S.V. Khare, D. Gall, First-principles phase diagram calculations for the rocksalt-structure quasibinary systems TiN–ZrN, TiN–HfN and ZrN–HfN, J. Phys. Condens. Matter 29 (2017) 035401.

[76] V. Adhikari, Z. Liu, N.J. Szymanski, I. Khatri, D. Gall, P. Sarin, S.V. Khare, First-principles study of mechanical and magnetic properties of transition metal (M) nitrides in the cubic M_4N structure, J. Phys. Chem. Solids 120 (2018) 197–206.

[77] F. Mouhat, F.X. Coudert, Necessary and sufficient elastic stability conditions in various crystal systems, Phys. Rev. B 90 (2014) 224104.

[78] J.F. Nye, Physical Properties of Crystals: Their Representation by Tensors and Matrices, Oxford University Press, 1985.

[79] G. Kresse, D. Joubert, From ultrasoft pseudopotentials to the projector augmented-wave method, Phys. Rev. B 59 (1999) 1758–1775.

[80] A. Togo, I. Tanaka, First principles phonon calculations in materials science, Scr. Mater. 108 (2015) 1–5.

[81] L. Ward, A. Dunn, A. Faghaninia, N. Zimmermann, S. Bajaj, Q. Wang, J. Montoya, J. Chen, K. Bystrom, M. Dylla, K. Chard, M. Asta, K.A. Persson, G.J. Snyder, I. Foster, A. Jain, Matminer: an open source toolkit for materials data mining, Comput. Mater. Sci. 152 (2018) 60–69.

[82] Y. Tian, B. Xu, Z. Zhao, Microscopic theory of hardness and design of novel superhard crystals, Int. J. Refract. Hard Met. 33 (2012) 93–106.

[83] P.E. Blöchl, O. Jepsen, O.K. Andersen, Improved tetrahedron method for Brillouin-zone integrations, Phys. Rev. B Condens. Matter 49 (1994) 16223–16233.

[84] F.W. Biegler-könig, R.F.W. Bader, T.H. Tang, Calculation of the average properties of atoms in molecules. II, J. Comput. Chem. 3 (1982) 317–328.

[85] G. Henkelman, A. Arnaldsson, H. Jónsson, A fast and robust algorithm for Bader decomposition of charge density, Comput. Mater. Sci. 36 (2006) 354–360.

[86] E. Sanville, S.D. Kenny, R. Smith, G. Henkelman, Improved grid-based algorithm for Bader charge allocation, J. Comput. Chem. 28 (2007) 899–908.

[87] V.L. Deringer, A.L. Tchougréeff, R. Dronskowski, Crystal orbital Hamilton population (COHP) analysis as projected from plane-wave basis sets, J. Phys. Chem. A 115 (2011) 5461–5466.

[88] R. Dronskowski, P.E. Blöchl, Crystal orbital Hamilton populations (COHP): energy-resolved visualization of chemical bonding in solids based on density-functional calculations, J. Phys. Chem. 97 (1993) 8617–8624.

[89] S. Maintz, V.L. Deringer, A.L. Tchougréeff, R. Dronskowski, Analytic projection from plane-wave and PAW wavefunctions and application to chemical-bonding analysis in solids, J. Comput. Chem. 34 (2013) 2557–2567.

[90] S. Maintz, V.L. Deringer, A.L. Tchougréeff, R. Dronskowski, LOBSTER: a tool to extract chemical bonding from plane-wave based DFT, J. Comput. Chem. 37 (2016) 1030–1035.

[91] S. Maintz, M. Esser, R. Dronskowski, Efficient rotation of local basis functions using real spherical harmonics, Acta Phys. Pol. B 47 (2016) 1165.

[92] A. Jain, S.P. Ong, G. Hautier, W. Chen, W.D. Richards, S. Dacek, S. Cholia, D. Gunter, D. Skinner, G. Ceder, K.A. Persson, Commentary: the materials project: a materials genome approach to accelerating materials innovation, APL Mater. 1 (2013) 011002.

[93] M. Kavitha, R. Rajeswarapalanichamy, K. Iyakutti, First principles study of structural, electronic superconducting and mechanical properties of titanium carbide, IJSER 5 (2014) 169–172.

[94] H.M. Tütüncü, S. Bağcı, G.P. Srivastava, A. Akbulut, Electrons, phonons and superconductivity in rocksalt and tungsten–carbide phases of CrC, J. Phys. Condens Matter 24 (2012) 455704.

[95] R.D. Shannon, D.B. Rogers, C.T. Prewitt, J.L. Gillson, Chemistry of noble metal oxides. III. Electrical transport properties and crystal chemistry of ABO_2 compounds with the delafossite structure, Inorg. Chem. 10 (1971) 723–727.

[96] R.W.G. Wyckoff, Cryst. Struct. 1 (1963) 85.

[97] P. Villars, L. Calvert, Pearson's Handbook of Crystallographic Data for Intermediate Phases, ASM, Cleveland, OH, 1985.

[98] B. Liu, X. Cheng, A metastable Cr carbide of NaCl structure formed by carbon-ion implantation into chromium films, J. Phys.: Condens. Matter 4 (1992) L265–L268.

[99] A.N. Christensen, The temperature factor parameters of some transition metal carbides and nitrides by single crystal x-ray and neutron diffraction, Acta Chem. Scand. 32 (1978) 89–90.

[100] E.K.K. Abavare, S. Dodoo, K. Uchida, G.K. Nkurumah-Buandoh, A. Yaya, A. Oshiyama, Indirect phase transition of TiC, ZrC, and HfC crystal structures, Phys. Status Solidi B 253 (2016) 1177–1185.

[101] D.L. Kepert, Aspects of the stereochemistry of eight-coordination, Prog. Inorg. Chem. (1978) 179–249.

[102] C.W. Haigh, Enumeration by pólya's theorem of the isomerism in eight-co-ordinate complexes in square antiprismatic, triangular dodecahedral and hendecahedral (bicapped trigonal prismatic) geometries, Polyhedron (1996) 605–643.

[103] P. Bhardwaj, Structural study of transition metal carbides, Acta Phys. Pol. A 122 (2012) 138–141.

[104] K. Kim, V. Ozoliŋš, A. Zunger, Instability of the high-pressure CsCl structure in most III-V semiconductors, Phys. Rev. B 60 (1999) R8449–R8452.

[105] O.C. Gagné, F.C. Hawthorne, Bond-length distributions for ions bonded to oxygen: results for the transition metals and quantification of the factors underlying bond-length variation in inorganic solids, IUCrJ 7 (2020) 581–629.

[106] K. Chen, S. Kamran, Bonding characteristics of TiC and TiN, Model. Numer. Simul. Mater. Sci. 3 (2013) 7–11.

[107] R. Janes, E.A. Moore, Metal-ligand bonding, R. Soc. Chem. (2004).

[108] E.A. Juarez-Arellano, et al., Formation of scandium carbides and scandium oxycarbide from the elements at high-(P, T) conditions, J. Solid State Chem. (2010) 975–983.

[109] E. Zhang, et al., A study on the kinetic process of reaction synthesis of TiC: Part I. Experimental research and theoretical model, Metall. Mater. Trans. A (1999) 1147–11514.

[110] L. Wu, et al., Understanding the mechanical properties of vanadium carbides: nano-indentation measurement and first-principles calculations, J. Alloy. Compd. (2013) 60–64.

[111] S.M. Schmuecker, et al., Synthesis of metastable chromium carbide nanomaterials and their electrocatalytic activity for the hydrogen evolution reaction, Dalton Trans. (2017) 13524–13530.

[112] K.H.J. Buschow, F.R. Boer, Physics of Magnetism and Magnetic Materials 7 Kluwer Academic/Plenum, New York, 2003.

[113] N.J. Szymanski, I. Khatri, J.G. Amar, D. Gall, S.V. Khare, Unconventional superconductivity in 3d rocksalt transition metal carbides, J. Mater. Chem. C 7 (2019) 12619–12632.

[114] A.L. Allred, E.G. Rochow, A scale of electronegativity based on electrostatic force, J. Inorg. Nucl. Chem. 5 (1958) 264–268.

[115] V.P. Zhukov, V.A. Gubanov, O. Jepsen, N.E. Christensen, O.K. Andersen, Calculated energy-band structures and chemical bonding in titanium and vanadium carbides, nitrides and oxides, J. Phys. Chem. Solids 49 (1988) 841–849.

[116] P. Soni, G. Pagare, S.P. Sanyal, Structural, high pressure and elastic properties of transition metal monocarbides: a FP-LAPW study, J. Phys. Chem. Solids 72 (2011) 810–816.

[117] Y. Lang, et al., Enhanced hardness in transition-metal monocarbides via optimal occupancy of bonding orbitals, ACS Appl. Mater. Interfaces (2021) 14365–14376.

[118] S.H. Jhi, et al., Electronic mechanism of hardness enhancement in transition-metal carbonitrides, Nature (1999) 132–134.

[119] N.R. Rathod, S.K. Gupta, P.K. Jha, First-principles structural, electronic and vibrational properties of zinc-blende zirconium carbide, Solid State Commun. 169 (2013) 32–36.

[120] S.F. Pugh, Relations between the elastic moduli and the plastic properties of polycrystalline pure metals, Philos. Mag. 45 (1954) 823–843.

[121] A. Teber, F. Schoenstein, F. Têtard, M. Abdellaoui, N. Jouini, Effect of SPS process sintering on the microstructure and mechanical properties of nanocrystalline TiC for tools application, Int. J. Refract. Hard Met. 30 (2012) 64–70.

[122] D. Bandyopadhyay, R.C. Sharma, N. Chakraborti, The Ti-Cr-C (titanium-chromium-carbon) system, J. Phase Equilib. 20 (1999) 325–331.

[123] Ohio-Supercomputer-Center. 〈http://osc.edu/ark:/19495/f5s1ph73〉.